Catalysis Today 178 (2011) 206–213

Contents lists available at ScienceDirect

Catalysis Today

journal homepage: www.elsevier.com/locate/cattod

Synergy effect of MgO and ZnO in a Ni/Mg–Zn–Al catalyst during ethanol steam reforming for H_2-rich gas production

Guangming Zeng, Qinghua Liu, Ruixue Gu, Lihong Zhang, Yongdan Li *

Tianjin Key Laboratory of Applied Catalysis Science and Technology and State Key Laboratory for Chemical Engineering (Tianjin University), School of Chemical Engineering and Technology, Tianjin University, Tianjin 300072, China

ARTICLE INFO

Article history:
Available online 27 August 2011

Keywords:
Hydrogen production
Ethanol
Steam reforming
Filamentous carbon
Hydrotalcite-like compound

ABSTRACT

Nickel based mixed oxide catalysts derived from Ni–Mg–Zn–Al hydrotalcite-like precursors are prepared and evaluated for H_2-rich gas production via ethanol steam reforming. It has been found that the catalyst properties (e.g. BET surface area, Ni dispersion and reducibility) and catalytic performance depend on the Mg:Zn molar ratio. MgO and ZnO have a synergetic effect. At 700 °C, the quaternary catalyst with a Mg:Zn ratio of 4 exhibits the highest H_2 yield and best stability, viz. no apparent variation of the product distribution over 100 h operation, whereas the ternary catalyst without Mg suffers severe coke accumulation after 7 h on-stream. Two types of carbon (filamentous and amorphous) are found deposited on the catalyst surface. The carbon deposited is dominated by filamentous carbon, which is likely originated from the decomposition of methane, and does not cause immediate deactivation.

1. Introduction

Hydrogen is considered to be the most viable energy carrier in the near future and facilitates the low carbon economy with the long-term potential to reduce pollutant emission [1–3]. Currently, large scale hydrogen production in industry is mainly from steam reforming (SR) of hydrocarbons (methane or naphtha oil) and coal gasification. Obviously, these processes are not sustainable nor CO_2 neutral. As an alternative, bio-ethanol produced renewably from many biomass sources, is a promising hydrogen carrier and has a great potential for contributing significantly toward short-to-medium-term targets of energy supply and environmental protection [4].

Thermodynamic analysis has proved that ethanol steam reforming (ESR) is entirely feasible to produce a high H_2 content syngas [5]. However, ESR is a complicated process that involves many reactions [6]. An excellent catalyst for ESR reaction requires a capability of breaking the C–C and C–H bonds and of promoting the subsequent formation of CO_2 and H_2 [7]. Although many metals [8–11] have been shown to be active in this process, Ni seems to be the most preferred active component. Nevertheless, the main challenges for the Ni-based catalyst as well as the noble metal-based ones are the deactivation due to sintering, coking and phase transformation [12]. Furthermore, ESR reaction for "on-board" and stationary application is expected to be carried out at lower temperatures than that of the commercialized reforming processes. Under these conditions, coking is encountered as a major obstacle.

It is believed that metal–support interaction contributes significantly to the catalyst activity and the resistance to carbon deposition. γ-Al_2O_3 is attractive for its high thermal stability and large surface area, but catalysts based on this support suffer severely from coking because of its strong acidity [13–15]. Therefore, the application of basic oxides (MgO, ZnO, La_2O_3 and Y_2O_3) [12–17] as supports and the addition of alkali species (Li, Na, and K) [18,19] into γ-Al_2O_3 have been conducted so as to improve the catalytic performance and minimize the coking. Recently, Mg–Al mixed oxide supported Ni catalyst was found to give superior H_2 and CO_x product selectivity, and improved catalyst stability in ESR compared to the single oxide (MgO or Al_2O_3) supported Ni catalysts [20]. Yang et al. [21] evaluated the effect of supports on ESR over Ni-based catalysts and found that the selectivity to hydrogen follows a decreasing order: Ni/ZnO ≈ Ni/La_2O_3 > Ni/MgO > Ni/γ-Al_2O_3. Most recently, ESR over ZnO/Al_2O_3 was ran by Chen et al. [22]. They found that a higher ZnO loading is better for suppressing CO production, preventing initial activity loss and improving long-term stability. Monzón et al. [23] also found that the presence of ZnO in Ni/Al_2O_3 gives rise to a selective catalyst with reduced rates of coking and methane formation. Abello et al. [7,24] carried out ESR over a Ni/Zn–Al catalyst prepared through a citrate sol–gel method and showed that the catalyst is very active and selective to H_2 and CO_2. Therefore, ZnO may promote the ESR via the H_2 and CO_2 pathway [25].

During the past four decades, much effort has been gone into assessing the potential use of hydrotalcite-like (HT-like) materials either as-synthesized or after thermal treatment as catalyst

* Corresponding author. Tel.: +86 22 27405613; fax: +86 22 27405243.
E-mail address: ydli@tju.edu.cn (Y. Li).

0920-5861/$ – see front matter © 2011 Elsevier B.V. All rights reserved.
doi:10.1016/j.cattod.2011.07.036

Table 1
The chemical compositions and interlayer distances of the HT-like precursors.

Samples	Ni:Mg:Zn:Al molar ratio	Mg:Zn ratio	Interlayer distance (Å)
NiMgAl	0.48:2.52:0.0:1.0	–	7.70
$NiMg_4Zn_1Al$	0.54:1.97:0.49:1.0	4:1	7.81
$NiMg_1Zn_1Al$	0.62:1.19:1.19:1.0	1:1	7.51
$NiMg_1Zn_4Al$	0.69:0.46:1.85:1.0	1:4	7.58
NiZnAl	0.74:0.0:2.26:1.0	–	7.66

[26–29]. For the application in heterogeneous catalysis, HT-like materials can be synthesized with several reducible bivalent (Ni, Co, Cu) and trivalent (Fe, Cr) cations in the structure together with the non-reducible ones (Mg, Zn, Al) serving as precursors of mixed oxide catalysts or supported metal catalysts [30]. Ni/Al_2O_3 catalysts derived from HT-like material have been studied in SR since 1970s [31]. HT-derived Ni/Mg–Al catalysts mainly composed of Ni–Mg–O solid solution phase exhibit high activity and stability in reforming of methane [32–34], ethanol [6,20], propane [35,36] and naphtha [37]. Zn–Al supported HT-derived Ni, Ni–Co and Ni–Cu catalysts are also used in SR processes. High activity and selectivity to H_2 and CO_2 in ethanol and acetic acid SR are reported over Ni and Ni–Co catalysts [38,39]. For Ni–Cu system, Ni-rich catalyst exhibits relatively high metal–support interaction in which Ni is somewhat decorated preferentially by Al and Zn [40].

MgO and ZnO are both basic and have close metal ionic radius (Mg^{2+}, 0.72 Å, Zn^{2+}, 0.74 Å) [41], but have different redox property. The major objective of this study is to discuss the synergetic effect of MgO and ZnO in HT-derived Ni/Mg–Zn–Al catalysts and further, to evaluate its influence on reforming activity and selectivity to CO_2.

2. Experimental

2.1. Catalyst preparation

The HT-derived catalysts were prepared by a co-precipitation technique. The Ni loading was fixed at 15 wt.% and the Mg:Zn molar ratio was varied as shown in Table 1. The atomic ratio, $x = (Ni^{2+} + Mg^{2+} + Zn^{2+})/Al^{3+}$ was fixed at 3/1. An aqueous solution containing nitrates of Ni^{2+}, Mg^{2+}, Zn^{2+} and Al^{3+} was added slowly with vigorous stirring into an aqueous solution of sodium carbonate (1.0 mol L^{-1}). By adjusting the pH to 9.0, a heavy slurry was formed. After aging at 60 °C for 12 h, the slurry was cooled down to room temperature, filtrated, and washed with de-ionized water. The material was dried overnight at 120 °C and then calcined in a muffle furnace at 600 °C for 6 h with a ramp of 5 °C min^{-1}. The formed powder was pressed, crushed and sieved to particles of 60–80 mesh.

2.2. Catalyst characterization

BET surface areas were measured using an Autosorb-1C-MS (Quantachrome) instrument by adsorption of nitrogen at −196 °C with 200 mg of sample previously degassed at 300 °C for 2 h under high vacuum.

X-ray diffraction (XRD) patterns were obtained at room temperature using a Rigaku D/max 2500 v/pc instrument (Rigaku Corp., Japan) with Cu Kα radiation, 40 kV and 200 mA power. The step-scans were taken over the range of 2θ from 5 to 90° in steps of 0.02° and the intensity data for each one were collected for 0.15 s. JADE5 software was utilized for data analysis.

Temperature-programmed reduction (TPR) was performed on a ThermoFinnigan TPD/R/O 1100 reaction system at a heating rate of 10 °C min^{-1} from room temperature to 900 °C using a mixture of 5 vol% H_2/N_2 as reduction gas. The H_2 consumption was measured by a TCD.

H_2-chemisorption was conducted with the Autosorb-1C-MS (Quantachrome). The calcined catalyst sample (about 0.1 g) was reduced at 700 °C for 2 h in H_2/N_2 and characterized at 40 °C. The adsorption isotherm was measured between 16 and 40 mmHg. The amount of hydrogen chemisorbed is determined by extrapolating the linear part of the isotherms to zero pressure.

Temperature-programmed oxidation (TPO) was performed on a ThermoFinnigan TPD/R/O 1100 reaction system at a heating rate of 10 °C min^{-1} from room temperature to 900 °C using a mixture of 6 vol% O_2/He as oxidation gas. Approximately 30 mg of used catalyst was employed for each experiment. Thermal gravimetric (TG) analysis was done with air as oxidant using a Perkin Elmer Pyris Diamond TG-DTA. Approximately 30 mg of used catalyst was heated from room temperature to 900 °C at a ramp of 10 °C min^{-1} and the weight change was measured. High resolution transmission electron microscopy HRTEM images were recorded on a FEI Tecnai G2 F20 equipment operating at 200 kV. Specimens were prepared by ultrasonically suspending the sample in ethanol. A drop of the suspension was applied onto a copper grid supported transparent carbon foil and dried in air before analysis.

2.3. Catalyst testing

ESR reactions were carried out in a fixed bed stainless-steel tubular reactor, operating at atmospheric pressure, loaded with 200 mg of catalyst mixed with 1.0 g of quartz particles (both in 60–80 mesh). The catalyst was pre-reduced at 700 °C for 2 h with 30 ml min^{-1} H_2 prior to the introduction of vapor phase ethanol–water feed mixture. A 3:1 molar ratio of H_2O:C_2H_5OH solution was fed by a micro-pump at a rate of 4 ml h^{-1} to the vaporizer, which was maintained at 200 °C. 20 ml min^{-1} N_2 was added to the vaporized reactant feed as an internal standard to aid in the analysis. The feed and reaction products were analyzed every 15 min during several hours, 2 h for temperature dependent and 7 h for coke formation experiments, and averaged using a PerkinElmer Clarus 500 GC equipped with TCD and FID detectors.

3. Results

3.1. Characterization

3.1.1. X-ray diffraction pattern

The XRD patterns of the as-prepared HT-like precursors are presented in Fig. 1. Obviously, all the samples show the characteristic diffractions of HT-like structure. Although the peak intensities show some differences between the patterns, no other oxide or hydroxide phases were detected. The three quaternary precursors ($NiMg_4Zn_1Al$, $NiMg_1Zn_1Al$ and $NiMg_1Zn_4Al$) look less crystalline than the ternary samples (NiMgAl and NiZnAl), as proofed by the broadness of the peaks. The interlayer distance, as measured from the position of the first peak ((0 0 3) peak) at the left hand side is 7.70 Å for precursor NiMgAl, a little larger than that of precursor NiZnAl (7.66 Å). However, the other three quaternary precursors are 7.81 Å, 7.51 Å and 7.58 Å respectively, exhibiting a non-monotonic trend along with the increase of the Zn content, as listed in Table 1.

After calcination at 600 °C, the HT-like precursor was transformed into metal oxides. As illustrated in Fig. 2, the Zn-containing samples are much more complex in phase composition than that of sample NiMgAl, which is in line with what have been reported recently [42]. The diffraction pattern of NiMgAl proves the formation of the Ni–Mg–O solid solution showing the major structural characteristics of the MgO phase. However, in the cases

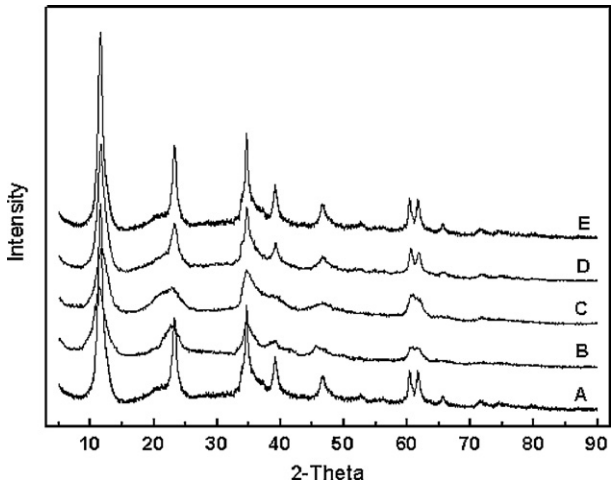

Fig. 1. XRD patterns of the hydrotalcite-like precursors: (A) NiMgAl, (B) $NiMg_4Zn_1Al$, (C) $NiMg_1Zn_1Al$, (D) $NiMg_1Zn_4Al$, (E) NiZnAl.

with Zn addition, the wurtzite type phase, ZnO, and the spinel phase, $ZnAl_2O_4$, appear and their peak intensities improve with the increase of the Zn content. For $NiMg_1Zn_1Al$, peaks of NiO, MgO, ZnO, and $ZnAl_2O_4$ phases are observed. Further increase the Zn content, the contribution of the ZnO and spinel phases increase while the intensities of the MgO peaks reduce. Besides, XRD diffraction peaks of MgO and NiO phases at around 43° and 62° are shifted to higher 2θ angles, for 0.36° and 0.56°, respectively.

3.1.2. BET and H_2-chemisorption

The BET surface area, pore volume and average pore diameter of the calcined catalysts are listed in Table 2. It shows that the pore structure is dependent on the Zn content [43]. All catalysts are mesoporous and have high surface area. The addition of Zn results in a decrease in surface area but an increase in average pore diameter.

The Ni dispersion and Ni surface area are also reported in Table 2. It is noteworthy that all samples have high Ni surface area and good Ni dispersion after reduction. The Ni dispersion and surface area follow a same order: $NiMg_4Zn_1Al$ > NiMgAl > $NiMg_1Zn_4Al$ > $NiMg_1Zn_1Al$ > NiZnAl. $NiMg_4Zn_1Al$ exhibits the highest Ni dispersion, 3.02%, and largest Ni surface area, 20.1 $m^2\,g^{-1}$, whereas the sample without Mg (NiZnAl) has the lowest Ni dispersion and Ni surface area.

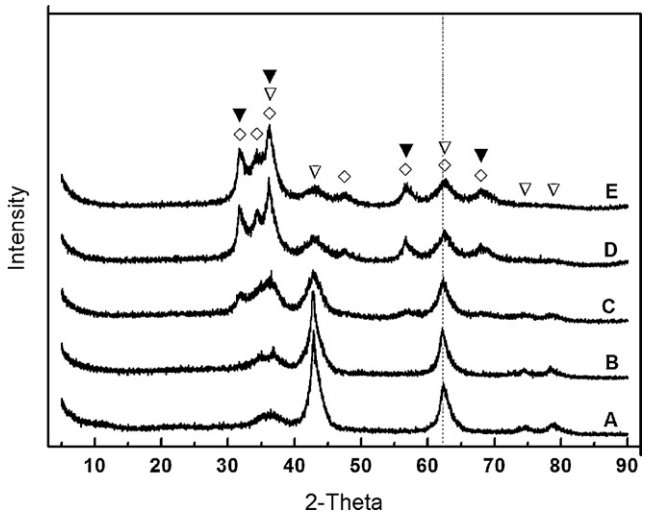

Fig. 2. XRD patterns of the mixed oxide samples after calcination at 600 °C: (A) NiMgAl; (B) $NiMg_4Zn_1Al$; (C) $NiMg_1Zn_1Al$; (D) $NiMg_1Zn_4Al$; (E) NiZnAl. (▽) NiO, MgO, Ni–Mg–O; (▼) $ZnAl_2O_4$; (◇) ZnO.

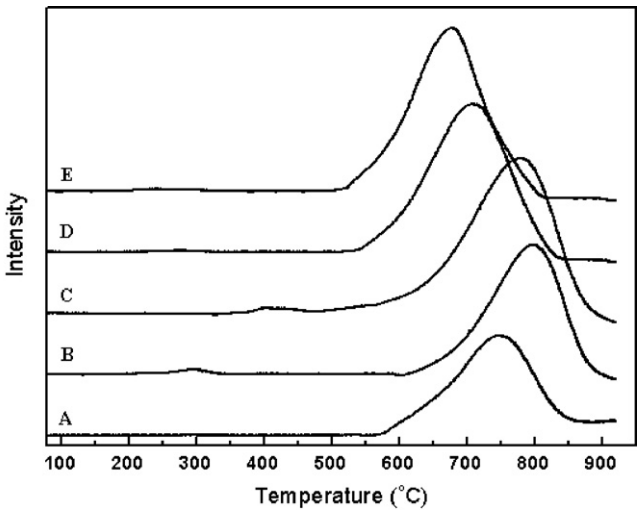

Fig. 3. TPR profiles of the mixed oxide samples after calcination at 600 °C: (A) NiMgAl; (B) $NiMg_4Zn_1Al$; (C) $NiMg_1Zn_1Al$; (D) $NiMg_1Zn_4Al$; (E) NiZnAl.

3.1.3. Temperature-programmed reduction

The TPR profiles of mixed oxides, shown in Fig. 3, reveal that all the main reduction peaks of the samples are above 650 °C and that the support composition has a significant effect on the reducibility of Ni. The samples with appropriate Mg:Zn ratios ($NiMg_4Zn_1Al$ and $NiMg_1Zn_1Al$) are more resistant to reduction than the ternary catalysts (NiMgAl and NiZnAl) and the other Zn-containing sample ($NiMg_1Zn_4Al$). The reducibility of Ni in the samples decreases in an order: NiZnAl > $NiMg_1Zn_4Al$ > NiMgAl > $NiMg_1Zn_1Al$ > $NiMg_4Zn_1Al$. Typically, the reduction of the unsupported NiO shows a single broad peak located at approximately 364 °C, spanning 250–430 °C [20]. It is apparent that very small amount of free NiO exists as a separate phase in $NiMg_4Zn_1Al$ catalyst which evolves a small hydrogen consumption peak at 290 °C, while $NiMg_1Zn_1Al$ exhibits this peak at 420 °C. These two samples have separate NiO phase in close interaction with the other phases, i.e., MgO, ZnO and $ZnAl_2O_4$. Moreover, it is interesting to note that the addition of Zn firstly shifts the main broad reduction peak to high temperature, viz. $NiMg_4Zn_1Al$ is the most difficult one for reduction.

3.2. Catalytic performance

3.2.1. Effect of reaction temperature

Fig. 4 plots the temperature dependence of the product distribution during ESR over the different catalysts. Ethanol and the possible intermediates like acetaldehyde, ethylene and acetone are entirely converted to H_2 and C_1 products above 400 °C, indicating the high activity of the Ni catalysts.

For NiMgAl, the H_2 yield increases with the increase of the temperature and reaches the maximum value of 5.07 mol/(mol ethanol) at 700 °C. After this temperature, the H_2 yield decreases slowly with the further increase of temperature. The curves of CO_2 and CH_4 yields show an initial increase at temperatures <500 and 450 °C respectively, and then a quick decrease until 700 °C. Further increase the temperature, both of these two yields reach their relative constant low value, though actually the CH_4 yield is negligible. The CO yield presents an opposite variation trend to those of CO_2 and CH_4, that it decreases quickly before 500 °C and then increases apparently until 700 °C. After 700 °C, the CO yield approaches a constant value. The maxima of CO_2 yield located at 500 °C is 1.0 mol/(mol ethanol), while that of CH_4 yield at 450 °C

Table 2
Textural properties of the HT-derived mixed oxides and the reduced catalysts.

Samples	BET ($m^2\ g^{-1}$)	Pore volume ($cm^3\ g^{-1}$)	Average pore diameter (nm)	Ni dispersion (%)	Surface area of Ni ($m^2\ g^{-1}$)
NiMgAl	209.7	0.46	8.79	1.99	13.2
$NiMg_4Zn_1Al$	185.2	0.40	8.70	3.02	20.1
$NiMg_1Zn_1Al$	185.9	0.49	10.71	1.67	11.2
$NiMg_1Zn_4Al$	121.3	0.35	11.69	1.68	11.2
NiZnAl	104.1	0.32	12.24	1.39	9.25

is 0.89 mol/(mol ethanol). At the same temperature as that of CO_2, CO yield presents the minimum value, 0.21 mol/(mol ethanol). It is interesting to note that, the three yield curves of CO, CO_2 and CH_4 almost meet at around 600 °C.

The Zn containing catalysts show similar trends for the yields of products, however, with different position and curvature of the curves. Several remarkable features of the catalytic performances of the samples should be noted: (1) for Zn-containing samples, the curves of CO, CO_2 and CH_4 yields do not meet at the same point, but the CO and CH_4 curves meet at a temperature region of 550–600 °C, lower than that of the curves of CO and CO_2 (600–650 °C) meet; (2) the yield of H_2 shows a minima at 450 °C for samples $NiMg_1Zn_1Al$, $NiMg_1Zn_4Al$ and NiZnAl, whereas $NiMg_4Zn_1Al$ has a slight maximum; (3) at temperatures higher than 700 °C, the H_2 yields of $NiMg_4Zn_1Al$ and $NiMg_1Zn_1Al$ curve down, while $NiMg_1Zn_4Al$ and NiZnAl show relatively stable yields in the same temperature range; (4) the yields of H_2 and CH_4 show opposite trends for all samples, however, the variation of CH_4 yield cannot take account of all the H_2 improved since water conversion varies along with the increase of temperature.

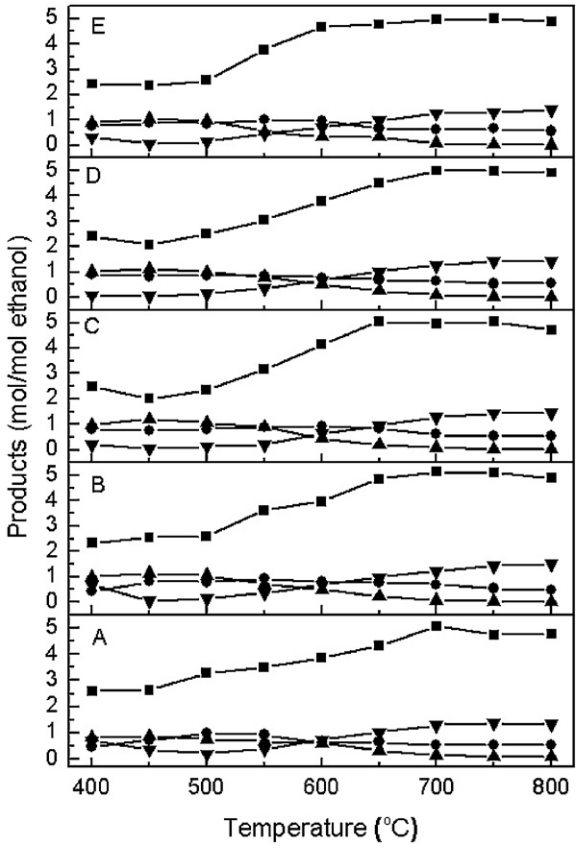

Fig. 4. Effect of reaction temperature on the yields of products during ESR reaction over Ni-based catalysts: (A) NiMgAl; (B) $NiMg_4Zn_1Al$; (C) $NiMg_1Zn_1Al$; (D) $NiMg_1Zn_4Al$; (E) NiZnAl. (■) H_2; (●) CO_2; (▲) CH_4; (▼) CO.

The samples with a Mg:Zn ratio of 4 ($NiMg_4Zn_1Al$) and 1/4 ($NiMg_1Zn_4Al$) achieve their maximum H_2 yields at 700 °C, 5.15 and 5.0 mol/(mol ethanol) respectively, while that of $NiMg_1Zn_1Al$ and NiZnAl appear at 750 °C, 5.05 and 5.01 mol/(mol ethanol) respectively. Among all the Zn-containing catalysts, even though the yields of CO increase significantly between 500 and 750 °C, as shown in Fig. 4(B)–(E), CO_2 is the predominant CO_x products until 600 °C. However, as an undesired by-product, CH_4 yield exhibits a slight maximum at 450 °C followed by a continued decrease until almost zero.

In summary, high H_2 yield, around 5.0 mol/(mol ethanol) and low CH_4 production especially for Zn-containing samples at <0.11 mol/mol ethanol, are obtained at temperatures between 700 and 750 °C, while the yield of CO_2 acts as the predominant CO_x species until 600 °C. Among all the five samples, the one with a Mg:Zn ratio of 4 ($NiMg_4Zn_1Al$) achieves the highest H_2 yield, 5.15 mol/(mol ethanol), at 700 °C as well as a highest CO_2 production at the same temperature.

3.2.2. Coke formation

The average product distribution at 700 °C for ESR during 7 h on-stream is shown in Table 3. The C1 product (CO, CO_2 and CH_4) distribution is similar for all the catalysts. The CO yield is almost the same for all the Zn containing catalysts, being close to 1.3 mol/(mol ethanol). The H_2 yield varied from 4.82 to 4.94 mol/(mol ethanol) with no apparent correlation with the catalyst composition. Nevertheless, the Zn content shows a relatively obvious effect on the CO_2 and CH_4 yields. $NiMg_4Zn_1Al$ catalyst is highly selective for CO_2 formation. However, this selectivity fluctuates with the further increase of Zn content, while that of CH_4 shows an opposite variation trend.

Examinations of the used catalyst tell that carbonaceous species are present on all the catalysts after reaction at 700 °C. TG analysis shows that the amount of carbon deposited increases from 18.97 wt.% to 55.05 wt.% with the increase of Zn content, as listed in Table 4. XRD patterns of the used catalysts in Fig. 5 verify this trend, at which the aboard diffraction peak at $2\theta = 26°$ proves the formation of coke. The intensity of this peak increases with the increase of the Zn content. However, the peak is widened for all samples indicating a poor crystallinity of the carbon phase.

The TPO curve of $NiMg_4Zn_1Al$ tested at 700 °C is plotted in Fig. 6. Two main peaks with an area ratio close to 1:8 are presented in the curve. The first one locates at around 380 °C, being likely due to the combustion of poorly polymerized, H-rich coke attached on the Ni particles [44,45]. The second but much larger peak locates in the

Table 3
Effect of support composition on yields of ethanol steam reforming reaction (mol/mol ethanol) (T = 700 °C, H_2O/C_2H_5OH = 3, time = 7 h, flow rate of mixed solution = 4 ml h^{-1}).

Samples	H_2	CO_2	CH_4	CO
NiMgAl	4.83	0.56	0.11	1.33
$NiMg_4Zn_1Al$	4.94	0.62	0.10	1.28
$NiMg_1Zn_1Al$	4.82	0.56	0.12	1.31
$NiMg_1Zn_4Al$	4.84	0.57	0.12	1.31
NiZnAl	4.86	0.60	0.11	1.29

Table 4
Coke accumulated on the HT-derived mixed oxide catalysts after 7 and 100 h on stream.

Samples	Coke formation (wt%)
NiMgAl	18.97
$NiMg_4Zn_1Al$	21.77/27.18[a]
$NiMg_1Zn_1Al$	34.59
$NiMg_1Zn_4Al$	38.53
NiZnAl	55.05

[a] Value examined after 100 h time-on-stream. Other values are after 7 h on stream.

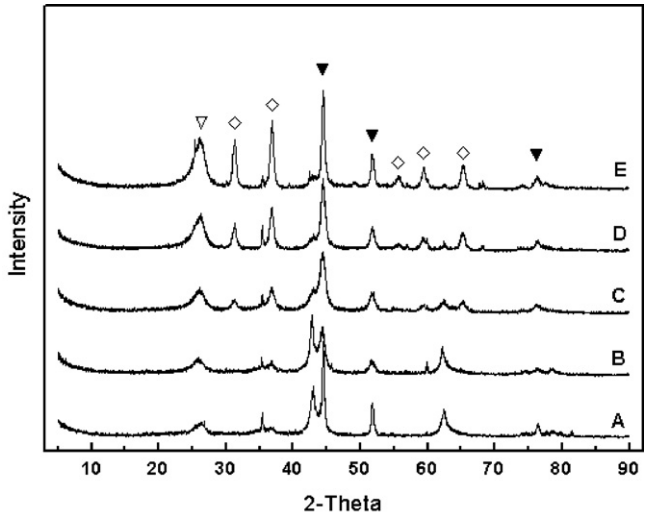

Fig. 5. XRD patterns of the used catalysts after experiments performed at 700 °C for 7 h: (A) NiMgAl; (B) $NiMg_4Zn_1Al$; (C) $NiMg_1Zn_1Al$; (D) $NiMg_1Zn_4Al$; (E) NiZnAl. (▽) Carbon; (▼) Ni; (◊) $ZnAl_2O_4$.

temperature range of 500–850 °C, which should be attributed to the oxidation of coke deposited with a degree of graphitization, probably filamentous carbon [46]. The HR-TEM images of $NiMg_4Zn_1Al$ catalyst after ESR reaction at 700 °C are given in Fig. 7. The images display the presence of a large amount of carbon deposits, which fully covers the surface of the catalyst. While both amorphous and filamentous carbons are observed, the filamentous type is obviously dominant, and has a highly graphitic nature as revealed by the regular layered structure observed in Fig. 7(b). The diameter of the filamentous carbon is in 10–15 nm, which is believed to be related to the metal particle size [47,48], and the arrangement of

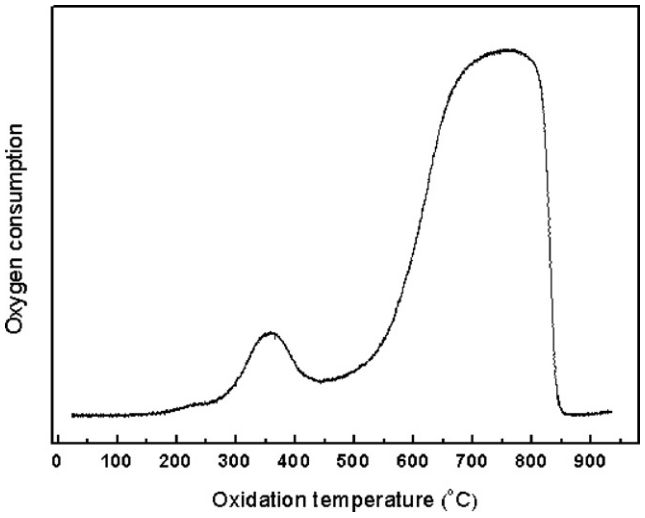

Fig. 6. A TPO profile of $NiMg_4Zn_1Al$ catalyst after reaction for 7 h.

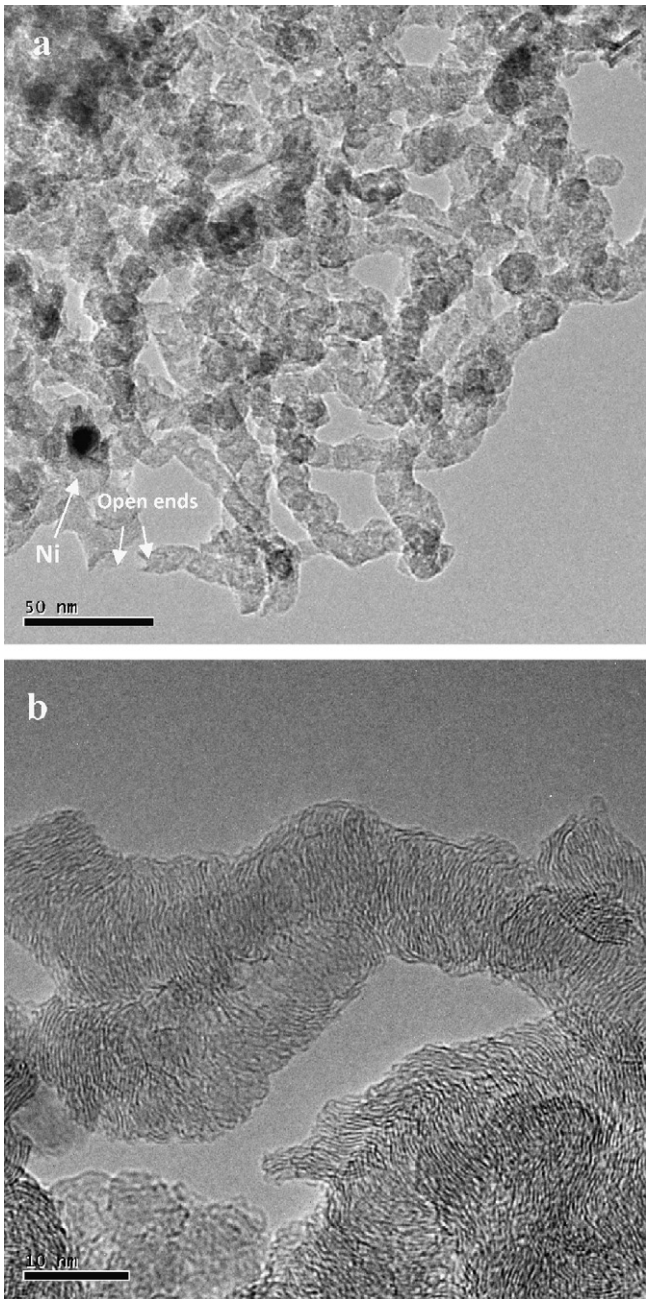

Fig. 7. HR-TEM images of the used catalyst ($NiMg_4Zn_1Al$) after reaction at 700 °C for 7 h.

the graphite layer is platelet. Most importantly, Ni particles appear in two spatial arrangements: (1) dispersed on the support surfaces and in this case, amounts of coke deposited covered the metal particle and support exterior, or (2) alternately, a fraction of Ni particles have been lifted off the support host surface (as illustrated in Fig. 7(a), several carbon filaments are characterized by showing Ni particles on top or an open end where a Ni particle became detached) and in this case, those Ni particles initiated the growth of the filamentous carbon.

3.2.3. Long-term stability

Fig. 8 presents the yields of H_2, CO, CO_2, and CH_4 in the outlet streams of $NiMg_4Zn_1Al$ catalyst as a function of time-on-stream at 700 °C. It can be seen that this catalyst exhibited a rather stable performance during 100 h on-stream. The amount of carbon deposited is 27.18% (g_{coke}/g_{cat}), only slightly larger than that after

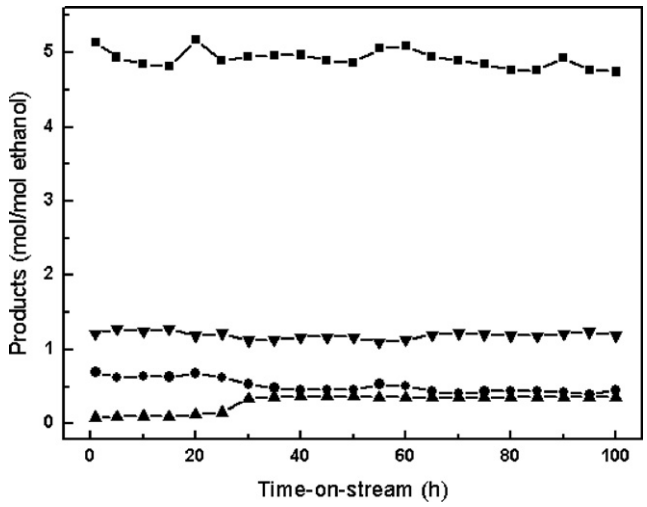

Fig. 8. Stability test of $NiMg_4Zn_1Al$. (■) H_2; (●) CO_2; (▲) CH_4; (▼) CO (T = 700 °C, H_2O/C_2H_5OH = 3, time = 100 h, flow rate of mixed solution = 4 ml h^{-1}).

7 h on-stream. The major variation of the gas product distribution with reaction time is that the CH_4 yield progressively increases, from 0.09 to 0.34 mol/mol ethanol, at the expense of lowering CO_2, from 0.70 to 0.53 mol/mol ethanol, during the first 30 h. The pressure drop of the reactor was also seen slightly increase during the 100 h operation, indicating the occurrence of snail-paced coking on the catalyst surface.

4. Discussion

4.1. Catalyst property

The XRD patterns show a general trend related to the chemical composition, as evidenced from the broadened XRD peaks in Fig. 1. Mg^{2+} and Zn^{2+} has similar ionic radius, i.e. 0.72 Å and 0.74 Å., respectively. The co-existence of these ions in HT-like structure is possible. However, the co-incorporation of Zn and Mg in the quaternary precursors distorts the layer structure as compared to that of the ternary precursors, resulting in broadened peaks and lowered crystallinity, as well as varied interlayer distances. Moreover, after calcination, the increasing Zn content shifts the reflection peaks of NiO and MgO to higher 2θ angle, which evidences the incorporation of Zn in MgO lattice and possibly formation of ZnO–MgO (–NiO) solid solution [49].

The high total Ni loading (15 wt.%), but low Ni surface area as shown in Table 2 implies that a considerable amount of Ni in the catalyst bulk is not exposed, and therefore, ineffective for catalysis. A small amount of larger Zn^{2+} ion addition ($NiMg_4Zn_1Al$) may distort the layered structure of HT-like precursor, contributing to form more open porous structure, improving metal surface area. However, the Ni dispersion calculated from H_2-chemisorption is very small and the calculated particle size is large, which is contradictory to that seen in the HR-TEM images. HR-TEM images exhibit some Ni particles have sizes of around 12 nm and the diameters of the filamentous carbon are in 10–15 nm, which is also close to the Ni particle size [47,48,50]. This discrepancy is ascribed to the partial reduction and inaccessibility of the metal. The H_2 uptake could be also particle size-dependent [51]. Further increase of Zn content leads to a decrease of the metal dispersion, which implies that the interaction of NiO with ZnO and/or $ZnAl_2O_4$ is not as strong as that of NiO with MgO in solid solution.

In the TPR curves, the NiMgAl catalyst shows a broad Ni^{2+} reduction peak at around 750 °C, which is a typical feature of catalysts derived from Ni–Mg–Al HT-like precursors [5,20,32,37], corresponding to the extraction of Ni from the bulk solid-solution (Ni–Mg–O) or spinel phases ($NiAl_2O_4$). The weak peaks at low temperature shown in Fig. 3(B) and (C) are associated with the reduction of NiO that is in weak interaction with the support. Additionally, the high temperature reduction peaks apparently shift forward or backward with the addition of Zn, which is related to the competing interaction of ZnO, $ZnAl_2O_4$ and MgO with NiO. Coleman et al. [20] reported the study of Ni/Mg–Al mixed oxide materials with different content of Al and Mg and concluded that the increase of Al content in Mg–Al mixed oxide increased the NiO reducibility, with the reduction peak shifting to lower temperature, ascribing to the enhancing interaction of MgO and Al_2O_3 and correspondingly weakening the interaction of MgO and NiO. In this work, for NiMgAl catalyst, most Ni is incorporated into the highly stable Ni–Mg–O solid solution, resulting in the unique high reduction peak. The addition of Zn into the Ni/Mg–Al mixed oxide leads to the formation of $ZnAl_2O_4$ phase (Fig. 2), reducing the interaction of MgO with Al_2O_3 in Mg(Ni, Al)O phase or the possible $MgAl_2O_4$ spinel phase, and consequently, enhances the NiO–MgO interaction, thus shifting the main reduction peak to higher temperature. However, in cases with further increase of Zn content, the predominant interaction would be NiO with ZnO and/or $ZnAl_2O_4$, which is not as strong as that of NiO with MgO. Therefore, the catalyst with a Mg:Zn ratio of 4, i.e. $NiMg_4Zn_1Al$, achieves the highest reduction temperature. Summing up, the TPR and XRD profiles shown in Figs. 2 and 3 suggest that NiO may have a stronger interaction with MgO than ZnO and $ZnAl_2O_4$, and a synergetic effect of MgO (interacting with NiO to form Ni–Mg–O solid solution) and ZnO (competing Al_2O_3 from MgO to form $ZnAl_2O_4$ spinel) induces the hardest reducibility of active metal species in $NiMg_4Zn_1Al$ catalyst.

4.2. Catalytic performance

4.2.1. Effect of reaction temperature

ESR reaction is complex because it has a lot of possible reaction pathways. The following reactions may take place simultaneously or successively. However, the contribution to the product distribution by each reaction depends on the reaction conditions.

$$C_2H_5OH \rightarrow CH_3CHO + H_2 \quad \Delta H^\circ = 68\ kJ\ mol^{-1} \tag{1}$$

$$C_2H_5OH \rightarrow C_2H_4 + H_2O \quad \Delta H^\circ = 45\ kJ\ mol^{-1} \tag{2}$$

$$C_2H_5OH \rightarrow 1.5CH_4 + 0.5CO_2 \quad \Delta H^\circ = -74\ kJ\ mol^{-} \tag{3}$$

$$CH_3CHO \rightarrow CH_4 + CO \quad \Delta H^\circ = -19\ kJ\ mol^{-1} \tag{4}$$

$$CH_3CHO + H_2O \rightarrow 2CO + 3H_2 \quad \Delta H^\circ = 187\ kJ\ mol^{-1} \tag{5}$$

$$C_2H_4 + 2H_2O \rightarrow 2CO + 4H_2 \quad \Delta H^\circ = 210\ kJ\ mol^{-1} \tag{6}$$

$$CH_4 + H_2O \leftrightarrow CO + 3H_2 \quad \Delta H^\circ = 206\ kJ\ mol^{-1} \tag{7}$$

$$CH_4 + CO_2 \leftrightarrow 2CO + 2H_2 \quad \Delta H^\circ = 247\ kJ\ mol^{-1} \tag{8}$$

$$CO + H_2O \leftrightarrow CO_2 + H_2 \quad \Delta H^\circ = -41\ kJ\ mol^{-1} \tag{9}$$

Inspecting the experimental results in Fig. 4 and the thermodynamic equilibrium calculation shown in Fig. 9 [41], CO_2 and CH_4 are found to be the most occurring C-containing products at temperatures <600 °C, indicating that the prevalent reactions at low temperature region are ethanol dehydrogenation (1), acetaldehyde decomposition (4), methanation (reverse 7) and water–gas shift (WGS) (9) reactions, which also account for the low H_2 yield. While the reaction temperature raises, CH_4 yield decreases continuously until almost vanish, whereas the H_2 and CO contents increase concurrently, suggesting that dehydrogenation (1), decomposition (4), methane steam reforming (MSR) (7), methane dry reforming (MDR) (8) and reverse WGS (reverse 9) reactions are the major reactions. It seems likely that the temperature range of 550–650 °C is the transition region of WGS to reverse WGS, and methanation to MSR.

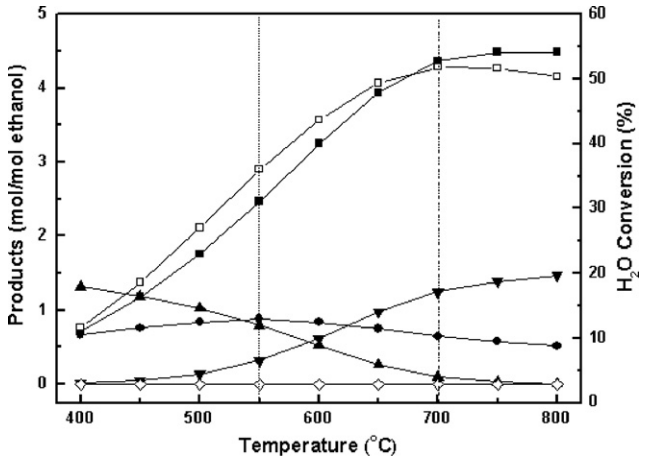

Fig. 9. Thermodynamic equilibrium product distribution of ethanol steam reforming as a function of temperature with a feed ratio of H_2O:C_2H_5OH = 3:1 at atmospheric pressure. (■) H_2; (●) CO_2; (▲) CH_4; (▼) CO; (◊) C; (□) H_2O.

Moreover, the H_2 yields show a decrease more or less after the maxima over the catalysts investigated, which probably relates to the contribution of MSR (7) and reverse WGS (reverse 9) to the conversion of H_2O since the theoretical highest H_2O conversion (52%) occurs at 700 °C.

4.2.2. Coke accumulation and stability

Coke formation on Ni catalysts involves several different routes and intermediates [52,53], the most probable reactions are:

$$2CO \leftrightarrow CO_2 + C \quad \Delta H^\circ = -172\,\text{kJ mol}^{-1} \tag{10}$$

$$C_2H_4 \leftrightarrow 2C + 2H_2 \quad \Delta H^\circ = -53\,\text{kJ mol}^{-1} \tag{11}$$

$$CH_4 \leftrightarrow C + 2H_2 \quad \Delta H^\circ = 75\,\text{kJ mol}^{-1} \tag{12}$$

$$CO + H_2 \leftrightarrow C + H_2O \quad \Delta H^\circ = -131\,\text{kJ mol}^{-1} \tag{13}$$

The coke formation measurement after reaction (Table 3) and the stability (Fig. 8) test illustrate that the Ni catalysts used in this work have good activity in ESR reaction, and that an appropriate amount of Zn content leads to a high CO_2 production and excellent stability.

It shows in Table 4, that the increase of the Zn content promotes the amount of carbon accumulation. Bezen et al. [42] reported that the acid sites increase with the increase of Zn content in a Mg–Zn–Al mixed oxide. The increased number of acid sites as well as the decreased Ni dispersion in the Zn-containing catalysts may lead to the accumulation of more carbon. Compared to NiMgAl, even though much higher Ni dispersion and active metal surface area are achieved, a little more coke still accumulated on $NiMg_4Zn_1Al$ catalyst. The coke accumulation presented in Table 4 is well in line with that Mg is more favorable than Zn for limiting coke accumulation [6].

Applying the TPO peak assignments from literature as a basis, our TPO profile indicates the presence of amorphous carbon (H-rich) and filamentous carbon over the $NiMg_4Zn_1Al$ catalyst after running SR for 7 h and following exposure to oxidative reaction. In addition, the amount of amorphous carbon oxidized at around 380 °C is much small in the catalyst studied, which seems like more reactive and easier to be removed by gasification and may act as a kind of intermediate during the reforming reaction [48,51,54]. de Lima [55–57] and Song [58,59] recently demonstrated that the presence of active metal promotes the decomposition of dehydrogenated species (e.g., acetaldehyde, acetyl) and acetate species producing H_2, CO and CH_x species. The CH_x species formed may either block the metal–support interface and coating the active metal resulting in deactivation, or diffuse behind the particle, nucleating the growth of carbon filaments. In this study, the filamentous carbon lifts the Ni particles from the support, coinciding well with the results of Co-based catalyst [56,58], but this does not directly lead to catalyst deactivation. In case of an appropriate H_2O:C_2H_5OH ratio employed, enough of the active surface of both the support (filaments also act as a support) and metal remains exposed and accessible to reactants and intermediates, such that the catalyst deactivation rate is alleviated. Therefore, the catalyst can maintain its high activity even after 100 h, presenting only a small increase of coke accumulation compared to that of after 7 h on-stream which further suggests that the coke accumulation is rapid during the first several hours over the catalyst investigated.

5. Conclusions

A series of 15 wt.% Ni-loaded Mg–Zn–Al catalysts derived from HT-like precursors were prepared via a co-precipitation method. The catalyst with a Mg:Zn ratio of 4 distorted the HT-like structure, improved the Ni dispersion and the average pore diameter, enhanced the NiO–MgO interaction and thus made the mixed oxide NiO hard to reduce.

The catalytic performance test demonstrates that the catalysts used in this work are highly active and stable even with a stoichiometric feed composition. Ethanol and other possible reaction intermediates are completely reformed into H_2 and C_1 products even at 400 °C. The temperature range of 550–650 °C seems like the transition region of WGS to reverse WGS, and methanation to MSR. The quaternary catalyst with a Mg:Zn ratio of 4 ($NiMg_4Zn_1Al$) exhibits superior activity and the highest H_2 yield of 5.15 mol/(mol ethanol) at 700 °C. Significant amount of carbon, mostly filamentous with a small amount of H-rich amorphous, accumulated on the catalyst surface but did not directly lead to deactivation during 7 h at 700 °C. The catalyst with a Mg:Zn ratio of 4 maintains its excellent activity even after 100 h performance at 700 °C.

Acknowledgements

The financial support of NSF of China under contract numbers 20736007 and 21076150 are gratefully acknowledged. The work has been also supported by the Program of Introducing Talents to the University Disciplines under file number B06006, and the Program for Changjiang Scholars and Innovative Research Teams in Universities under file number IRT 0641.

References

[1] U.S. Department of Energy (Hydrogen Program), Hydrogen Posture Plan – An Integrated Research, Development and Demonstration Plan, Internet site: http://www.hydrogen.energy.gov/pdfs/hydrogen_posture_plan_dec06.pdf, 2006.
[2] Y.D. Li, J.L. Chen, Y.N. Qin, L. Chang, Energy Fuels 14 (2000) 1188–1194.
[3] G.M. Zeng, Y. Tian, Y.D. Li, Int. J. Hydrogen Energy 35 (2010) 6726–6737.
[4] A.N. Fatsikostas, X.E. Verykios, J. Catal. 225 (2004) 439–452.
[5] S. Liu, K. Zhang, L.N. Fang, Y.D. Li, Energy Fuels 22 (2008) 1365–1370.
[6] C. Resini, T. Montanari, L. Barattini, G. Ramis, G. Busca, S. Presto, P. Riani, R. Marazza, M. Sisani, F. Marmottini, U. Costantino, Appl. Catal. A 355 (2009) 83–93.
[7] M.N. Barroso, M.F. Gómez, L.A. Arrua, M.C. Abello, Appl. Catal. A 304 (2006) 116–123.
[8] A.F. Lucrédio, E.M. Assaf, J. Power Sources 159 (2006) 667–672.
[9] E. Nikolla, J. Schwank, S. Linic, J. Catal. 263 (2009) 220–227.
[10] A. Mastalir, A. Patzko, B. Frank, R. Schomacker, T. Ressler, R. Schlogl, Catal. Commun. 8 (2007) 1684–1690.
[11] T. Miyata, D. Li, M. Shiraga, T. Shishido, Y. Oumi, T. Sano, K. Takehira, Appl. Catal. A 310 (2006) 97–104.
[12] J. Sun, X.P. Qui, F. Wu, W.T. Zhu, Int. J. Hydrogen Energy 30 (2005) 437–445.
[13] A.N. Fatsikostas, D.I. Kondarides, X.E. Verykios, Catal. Today 75 (2002) 145–155.
[14] S. Freni, S. Cavallaro, N. Mondello, L. Spadaro, F. Frusteri, J. Power Sources 108 (2002) 53–57.

[15] S. Freni, S. Cavallaro, N. Mondello, L. Spadaro, F. Frusteri, Catal. Commun. 4 (2003) 259–268.
[16] X.Z. Deng, J. Sun, S.S. Yu, J.Y. Xi, W.T. Zhu, X.P. Qiu, Int. J. Hydrogen Energy 33 (2008) 1008–1013.
[17] W. Grzegorczyk, A. Denis, W. Gac, T. Ioannides, A. Machocki, Catal. Lett. 128 (2009) 443–448.
[18] F. Frusteri, S. Freni, V. Chiodo, L. Spadaro, G. Bonura, S. Cavallaro, J. Power Sources 132 (2004) 139–144.
[19] F. Frusteri, S. Freni, V. Chiodo, L. Spadaro, O.D. Blasi, G. Bonura, S. Cavallaro, Appl. Catal. A 270 (2004) 1–7.
[20] L.J.I. Coleman, W. Epling, R.R. Hudgins, E. Croiset, Appl. Catal. A 363 (2009) 52–63.
[21] Y. Yang, J.X. Ma, F. Wu, Int. J. Hydrogen Energy 7 (2006) 877–882.
[22] M.N. Chen, D.Y. Zhang, L.T. Thompson, Z.F. Ma, Int. J. Hydrogen Energy 36 (2011) 7516–7522.
[23] J.C. Rodríguez, E. Romeo, J.L.G. Fierro, J. Santamaría, A. Monzón, Catal. Today 37 (1997) 255–265.
[24] M.N. Barroso, M.F. Gómez, L.A. Arrua, M.C. Abello, React. Kinet. Catal. Lett. 97 (2009) 27–33.
[25] A.E. Galetti, GómezF M.F., L.A. Arrua, M.C. Abello, Appl. Catal. A 348 (2008) 94–102.
[26] J.R.H. Ross, Surf. Defect Prop. Solids 4 (1975) 34–67.
[27] J.L. Paulhiac, O. Clause, J. Am. Chem. Soc. 115 (1993) 11602–11603.
[28] K. Yamaguchi, K. Ebitani, T. Yoshida, H. Yoshida, K. Kaneda, J. Am. Chem. Soc. 121 (1999) 4526–4527.
[29] K. Motokura, N. Fujita, K. Mori, T. Mizugaki, K. Ebitani, K. Kaneda, J. Chem. Soc. 127 (2005) 9674–9675.
[30] D.P. Debecker, E.M. Gaigneaux, G. Busca, Chem. Eur. J. 15 (2009) 3920–3935.
[31] E.C. Kruissink, E.B.M. Doesburg, L.L. van Reijen, L.E. Alzamora, S. Orr, J.R.H. Ross, G. van Veen, Stud. Surf. Sci. Catal. 3 (1979) 143–157.
[32] A. Fonseca, E.M. Assaf, J. Power Sources 142 (2005) 154–159.
[33] T. Ohi, T. Miyata, D.L. Li, T. Shishido, T. Kawabata, T. Sano, K. Takehira, Appl. Catal. A 308 (2006) 194–203.
[34] A.I. Tsyganok, T. Tsunoda, S. Hamakawa, K. Suzuki, K. Takehira, T. Hayakawa, J. Catal. 213 (2003) 191–203.
[35] H.J. Lee, Y.S. Lim, N.C. Park, Y.C. Kim, Chem. Eng. J. 146 (2009) 295–301.
[36] A. Olafsen, A. Slagern, I.M. Dahl, U. Olsbye, Y. Schuurman, C. Mirodatos, J. Catal. 229 (2005) 163–175.
[37] F. Melo, N. Morlanés, Catal. Today 133 (2005) 383–393.
[38] L. Barattini, G. Ramis, C. Resini, G. Busca, M. Sisani, U. Costantino, Chem. Eng. J. 153 (2009) 43–49.
[39] G. Busca, U. Costantino, T. Montanari, G. Ramis, C. Resini, M. Sisani, Int. J. Hydrogen Energy 35 (2010) 5356–5366.
[40] S. Velu, K. Suzuki, M. Vijayaraj, S. Barman, C.S. Gopinath, Appl. Catal. B 55 (2005) 287–299.
[41] A. Roine, Outokumpu HSC Chemistry 4.0, Poris, Finland.
[42] M.C.I. Bezen, C. Breitkopf, J.A. Lercher, Appl. Catal. A 399 (2011) 93–99.
[43] A.C. Heredia, M.I. Oliva, C.I. Zandalazini, U.A. Agu, G.A. Eimer, S.G. Casuscelli, E.R. Herrero, C.F. Perez, M.E. Crivello, Ind. Eng. Chem. Res. 50 (2011) 6695–9703.
[44] J.L. Chen, X. Yang, Y.D. Li, Fuel 89 (2009) 943–948.
[45] C.H. Bartholomew, Appl. Catal. A 212 (2001) 17–60.
[46] S. Natesakhawat, R.B. Watson, X. Wang, U.S. Ozkan, J. Catal. 234 (2005) 496–508.
[47] A. Carrero, J.A. Calles, A.J. Vizcaino, Chem. Eng. J. 163 (2010) 395–402.
[48] A.R. Naghash, Z. Xu, T.H. Etsell, Chem. Matter. 17 (2005) 815–821.
[49] N. Pasupulety, G.L. Rempel, F.T.T. Ng, 22nd North American Catalysis Society Meeting, USA, 2011.
[50] Y.D. Li, D.X. Li, G.W. Wang, Catal. Today 162 (2011) 1–48.
[51] M.S. Fan, A.Z. Abdullah, S. Bhatia, Appl. Catal. B 100 (2011) 365–377.
[52] D.L. Trimm, Catal. Rev. Sci. Eng. 16 (1977) 115–189.
[53] D.L. Trimm, Appl. Catal. A 212 (2001) 153–160.
[54] Y. Nishiyama, Y. Tamai, J. Catal. 33 (1974) 98–107.
[55] S.M. de Lima, I.O. da Cruz, G. Jacobs, B.H. Davis, L.V. Mattos, F.B. Noronha, J. Catal. 257 (2008) 356–368.
[56] S.M. de Lima, A.M. da Silva, L.O.O. da Costa, U.M. Graham, G. Jacobs, B.H. Davis, L.V. Mattos, F.B. Noronha, J. Catal. 268 (2009) 268–281.
[57] S.M. de Lima, A.M. Silva, U.M. Graham, G. Jacobs, B.H. Davis, L.V. Mattos, F.B. Noronha, Appl. Catal. A 352 (2009) 95–113.
[58] H. Song, U.S. Ozkan, J. Catal. 261 (2009) 66–74.
[59] H. Song, X.G. Bao, C.M. Hadad, U.S. Ozkan, Catal. Lett. 141 (2011) 43–54.